Ensemble-based observation impact estimates using the NCEP GFS

Yoichiro Ota[1]
National Centers for Environmental Prediction/Environmental Modeling Center NCEP/NWS/NOAA, College Park, Maryland

John C. Derber
National Centers for Environmental Prediction/Environmental Modeling Center NCEP/NWS/NOAA, College Park, Maryland

Eugenia Kalnay
University of Maryland, College Park, Maryland

Takemasa Miyoshi
University of Maryland, College Park, Maryland
RIKEN Advanced Institute for Computational Science, Kobe, Japan

[1] *Corresponding author address*: Yoichiro Ota, National Centers for Environmental Prediction/Environmental Modeling Center, 5830 University Research Court, College Park, MD 20740.
E-mail: yoichiro.ota@noaa.gov

Abstract

The impacts of the assimilated observations on the 24 hour forecasts are estimated with the ensemble-based method proposed by Kalnay et al. using the ensemble Kalman filter (EnKF). This method estimates the relative impact of observations in data assimilation similarly to the adjoint-based method proposed by Langland and Baker but without using the adjoint model. It is implemented with the National Centers for Environmental Prediction (NCEP) Global Forecasting System (GFS) EnKF which has been used as a part of operational global data assimilation system at NCEP since May 2012. The result quantifies the overall positive impacts of the assimilated observations and the relative importance of the satellite radiance observations compared to other types of observations especially for the moisture variables. The method is also used to identify the cause of local forecast failure cases in the 24 hr forecasts. Data denial experiments of the observations identified as producing a negative impact observation sets reduce the forecast errors as estimated, validating the impact estimate.

1. Introduction

Estimating the observation impacts within the numerical weather prediction (NWP) system is an important step to improve the performance of the operational NWP. There have been substantial efforts to estimate the impact of the assimilated observations by carrying out data-denial experiments or the Observing System Experiments (OSE, e.g. Bouttier and Kelly 2001, Zapotocny et al. 2007, 2008). OSEs provide the nonlinear impacts on the accuracy of the forecasts with and without a certain set of observations. However, carrying out OSEs with various observation datasets is computationally very expensive. As an alternative, Langland and Baker (2004) proposed an approach to estimate the observation impacts on the forecasts without performing OSEs using the adjoint sensitivity analysis. This forecast sensitivity to observations approach can be performed with relatively low computational cost and provides the impact of each assimilated observations in a linear sense. It has been applied to several operational data assimilation systems and has been proven to be effective in estimating the observation impacts on the short-range forecasts and the performance of the data assimilation system (Zhu and Gelaro 2008, Cardinali 2009). However, it requires the adjoint operators of the forecast model and the data assimilation system. Liu and Kalnay (2008) and Li et al. (2010) proposed a similar method using the ensemble Kalman filter (EnKF) without the adjoint model. The ensemble-based approach is convenient for estimating the observation impacts in the ensemble-based data assimilation system since it uses the ensemble perturbations instead of the adjoint operators. Kunii et al. (2012) successfully applied the ensemble-based approach to estimate the impact of real observations with the Weather Research and Forecasting model using the Local Ensemble Transform Kalman Filter

(LETKF, Hunt et al. 2007) and estimated the impact of various observations on the Typhoon forecast. Kalnay et al. (2012) proposed an improved formulation of the Liu and Kalnay (2008) algorithm. It is simpler, more accurate (or makes fewer approximations), and can be applied on other EnKF and not just the LETKF.

In this study, observation impact estimates within the EnKF have been investigated. The formulation of Kalnay et al. (2012) was applied to the near operational global data assimilation settings using real observations. In this study it was applied to the NCEP Global Forecasting System EnKF (GFS/EnKF, Whitaker et al. 2008) with the observations assimilated in the NCEP operational global data assimilation system. The result provides the relative impacts of each observation type in the operational NWP context. We show that it can also be used as an effective tool to investigate the origin of local forecast failure cases that sometimes degrade the operational forecasts substantially. Section 2 introduces the formulation of the ensemble-based approach used in this study. Following section 3 with the experimental settings, section 4 presents the overall results and section 5 focuses on the evaluation of the origin of local forecast failures. Finally, section 6 provides a summary and discussion.

2. Ensemble-based formulation

We will estimate the forecast error reduction due to the assimilation of each observation. The forecasts from the analysis ($\overline{\mathbf{x}}_t^f$) and from the first guess ($\overline{\mathbf{x}}_t^g$) are verified against the analysis or any other values close to the truth ($\mathbf{x}_t^{truth}$) at forecast time *t*. We define the forecast errors as,

$$\mathbf{e}_t^f \equiv \overline{\mathbf{x}}_t^f - \mathbf{x}_t^{truth}, \quad \mathbf{e}_t^g \equiv \overline{\mathbf{x}}_t^g - \mathbf{x}_t^{truth}. \tag{1}$$

The overbars represent the ensemble mean and can be disregarded for the deterministic analysis and forecast. Following Langland and Baker (2004), forecast error reduction is defined as

$$\Delta e_t^{f-g} \equiv \frac{1}{2}\mathbf{e}_t^{f\mathrm{T}} C \mathbf{e}_t^f - \frac{1}{2}\mathbf{e}_t^{g\mathrm{T}} C \mathbf{e}_t^g = \frac{1}{2}\left(\mathbf{e}_t^f - \mathbf{e}_t^g\right)^{\mathrm{T}} C\left(\mathbf{e}_t^f + \mathbf{e}_t^g\right), \tag{2}$$

where C is the norm operator, defining the measure of the forecast error. The forecast error difference can be described as

$$\mathbf{e}_t^f - \mathbf{e}_t^g = \overline{\mathbf{x}}_t^f - \overline{\mathbf{x}}_t^g \approx \mathbf{M}\left(\overline{\mathbf{x}}_0^a - \overline{\mathbf{x}}_0^g\right) = \mathbf{M}\mathbf{K}\delta\mathbf{y}_o, \tag{3}$$

where $\overline{\mathbf{x}}_0^a$ and $\overline{\mathbf{x}}_0^g$ are the analysis and the first guess at time 0. $\mathbf{M}$ and $\mathbf{K}$ represent tangent linear forecast model and Kalman gain matrix. Here, $\delta\mathbf{y}_o \equiv \mathbf{y}_o - H\left(\overline{\mathbf{x}}_0^g\right)$, where $\mathbf{y}_o$ and H are the observation vector and nonlinear observation operator, is known as the vector of innovations. The forecast time t is assumed to be short, so that we can apply the tangent linear model. From (2) and (3), the forecast error reduction from the assimilation of observations is expressed as

$$\Delta e_t^{f-g} \approx \frac{1}{2}\left[\mathbf{M}\mathbf{K}\delta\mathbf{y}_o\right]^{\mathrm{T}} C\left(\mathbf{e}_t^f + \mathbf{e}_t^g\right) = \frac{1}{2}\delta\mathbf{y}_o^{\mathrm{T}}\mathbf{K}^{\mathrm{T}}\mathbf{M}^{\mathrm{T}} C\left(\mathbf{e}_t^f + \mathbf{e}_t^g\right). \tag{4}$$

This equation is used for the observation impact estimates based on the adjoint sensitivity. On the other hand, Kalman gain in the EnKF is

$$\mathbf{K} = \frac{1}{K-1}\mathbf{X}_0^a \mathbf{X}_0^{a\mathrm{T}} \mathbf{H}^{\mathrm{T}} \mathbf{R}^{-1}, \tag{5}$$

where K, $\mathbf{X}_0^a$, and $\mathbf{R}$ are the ensemble size, the matrix of analysis perturbations and the observation error covariance, respectively. (4) can also be described as

$$\begin{aligned}\Delta e_t^{f-g} &\approx \frac{1}{2(K-1)}\left[\mathbf{M}\mathbf{X}_0^a\left(\mathbf{H}\mathbf{X}_0^a\right)^{\mathrm{T}}\mathbf{R}^{-1}\delta\mathbf{y}_o\right]^{\mathrm{T}} C\left(\mathbf{e}_t^f+\mathbf{e}_t^g\right) \\ &\approx \frac{1}{2(K-1)}\delta\mathbf{y}_o^{\mathrm{T}}\mathbf{R}^{-1}\left(\mathbf{H}\mathbf{X}_0^a\right)\mathbf{X}_t^{f\mathrm{T}} C\left(\mathbf{e}_t^f+\mathbf{e}_t^g\right)\end{aligned} . \quad (6)$$

This equation is used for this study to estimate observation impacts. It is simpler and computationally more efficient than the original formulation of Liu and Kalnay (2008) and Li et al. (2010) and also can be easily applied to deterministic EnKFs other than the LETKF (Kalnay et al. 2012).

As the EnKF requires covariance localization when the number of degrees of freedom is much larger than the number of the ensemble members, the ensemble-based observation impact estimates also require localization in practical applications. Following Kalnay et al. (2012), we achieve this by computing the impact of *l* th observation on forecast at *j* th grid point as

$$\left(\Delta e_t^{f-g}\right)_{j,l} = \frac{1}{2(K-1)}\left(\delta\mathbf{y}_o\right)_l\left[\rho_j\mathbf{R}^{-1}\left(\mathbf{H}\mathbf{X}_0^a\right)\left(\mathbf{X}_t^{f\mathrm{T}}\right)_j C_{jj}\left(\mathbf{e}_t^f+\mathbf{e}_t^g\right)_j\right]_l , \quad (7)$$

where ρ_j is the localization function at grid point *j* for the *l* th observation. The localization function in (7) may be different from the one used in the EnKF analysis especially when the impact of the observations on the forecast moves during the forecast away from the initial location.

3. Experimental settings

Equation (7) is applied to the NCEP GFS/EnKF analysis and forecast ensembles. The horizontal resolution of the GFS in this experiment is T254 (about 55 km) and it has 64 sigma-p hybrid vertical layers up to 0.3 hPa. The serial Ensemble Square Root Filter (EnSRF, Whitaker and Hamill 2002) is applied for the EnKF analysis. EnKF employs 80

members and assimilates observations every 6 hours. The use of the ensembles allows one to measure the forecast error with both dry and moist total energy norm (Ehrendorfer et al. 1999) in the global domain and the verifications are made against its own analysis.

$$TE = \frac{1}{2}\frac{1}{S}\int_S\int_0^1 \left\{ \left(u'^2 + v'^2\right) + \frac{C_p}{T_r}T'^2 + \frac{R_d T_r}{P_r^{\,2}}p_s'^2 + w_q \frac{L^2}{C_p T_r} q'^2 \right\} d\sigma dS \,. \qquad (8)$$

Here u', v', T', p_s' and q' are the forecast errors of zonal wind, meridional wind, temperature, surface pressure and specific humidity, respectively. C_p, R_d and L are the specific heat at constant pressure, gas constant of dry air and latent heat of condensation per unit mass, respectively. T_r and P_r are reference temperature and pressure, respectively (we used 280 K and 10^5 Pa). w_q is 1 for moist total energy and 0 for dry total energy. Evaluation forecast time is chosen to be 24 hours.

The fifth order polynomial of Gaspari and Cohn (1999) is used as the covariance localization function with a cutoff length (where localization function becomes 0) at 2.0 scale heights for the vertical and 2000 km for the horizontal (corresponding to about 0.8 scale heights and 800 km with e-folding scales).

The localization scale for observation impact estimate is chosen to be the same as the EnKF analysis update. Since observation impacts evolve through the forecast, the localization function also needs to evolve. We tested both a fixed localization function as in the EnKF analysis and a mobile localization function with the center position moving with 0.75 times the average of analysis and forecast horizontal wind at each vertical level. Multiplicative inflation (Anderson, 2001) proportional to the spread reduction by analysis update is applied so that the amount of spread reduction becomes 15 % of the original

reduction. Also additive inflation using 0.32 times of randomly selected 24 and 48 hour forecast lagged differences is applied. These are the same settings as the EnKF analysis part of the NCEP operational global system. The assimilation cycles are performed from 00 UTC, January 1, 2012 to 18 UTC, February 8, 2012. The first week is discarded as operational assimilation system is still in spin-up mode and the last 1 month (from January 8 to February 7, 4 cycles per day, 124 cases) is used for the observation impact estimates. Forecast errors are verified against their own analysis. All observation types used in the NCEP operational global analysis (operational since May 2012, about 3.3 million observations in each analysis) except for satellite-based precipitation rate retrievals from TRMM/TMI are assimilated. Table 1 shows the observation types assimilated in this experiment. The same satellite radiance bias correction coefficients as the hybrid EnKF / 3DVAR experiment (the operational global data assimilation system since May 2012) are applied.

4. Results

a. The effect of a moving localization

First, the effect of localization on the observation impact estimates is examined. Figure 1 shows the time series of the total forecast error reduction. The actual forecast error reduction is verified against its own analysis. If the impact estimate was perfect, it would be identical with the actual error reduction. The error reduction is generally larger at 00 and 12 UTC than at 06 and 18 UTC because more conventional observations are available at 00 and 12 UTC. Observation impact estimates with the moving localization capture better the diurnal cycles than that with the fixed localization. Correlations of total

impact estimates to the true forecast error reduction are 0.318 with the fixed localization and 0.730 with the moving localization. The average impact estimation is larger for the moving localization. As suggested by Kalnay et al. (2012), special attention is required on the localization on the ensemble-based observation impact estimates. Although our approach is very simple and may not be optimal, the moving localization applied in this experiment works well in our real data assimilation problem. In the following sections, only the results with the moving localization are shown.

b. Estimated impacts of each observation type

Figure 2a shows the average 24 hour forecast error reduction estimates with the moist total energy contributed from each observation type during the experiment. Negative values correspond to the reduction of the forecast error due to the assimilation of the observations. All observation types except Ozone retrievals are estimated to reduce the forecast error on average in this period. In the EnKF, ozone observations are assimilated with a univariate covariance, i.e., only the ozone analysis is changed, with no impact on other variables at the analysis time, thus limiting the impact of the ozone observations on the forecast. For the overall impacts, AMSUA shows the largest contribution to the forecast error reduction. IASI and Aircraft are the second and the third, followed by radiosondes and AIRS.

The observation impact per observation is obtained by dividing the total impact by the observation count (Figure 2b). TCVital observations of tropical cyclones have extremely large impact per observation but the sample number is small (79 observations during the entire period and only in the Southern Hemisphere). Dropsonde observations also have very large impacts on average. Most of the dropsondes were deployed over the

Northeastern Pacific during the Winter Storm Reconnaissance program (Toth et al. 2002) led by National Oceanic and Atmospheric Administration (NOAA). This program aims to reduce the short-range forecast error of the strong extratropical cyclones using the observation targeting strategy (Bishop et al. 2001, Majumdar et al. 2002). The result suggests that this program is effective in reducing the forecast error. Other than these, conventional upper-air observations such as PIBAL and Radiosonde have large impacts per observation. Satellite scatterometer winds (ASCAT_Wind and WINDSAT_Wind) and marine surface observations also have relatively large impacts. Total contributions of those observations to the forecast error reduction are not so large, but those observations are more effective per observation.

Figure 3 is a similar plot as figure 2 but measured using the dry total energy. Comparing with figure 2, the impacts of the most satellite radiance observations are substantially reduced, especially for the MHS. PIBALs' impact per observation is also reduced. Those observations are estimated to have impacts mostly on the forecast of moisture variable. This is consistent with the facts that MHS is sensitive to the atmospheric moisture, and most pilot balloons are used in the India, Southeast Asia and Australia (summer in this period) where the atmospheric moisture is high. On the other hand, some observations such as GPSRO and MODIS wind have similar impacts with the moist and dry total energy indicating that they did not impact the moisture forecast. Most of the assimilated GPSRO observations measure the atmosphere above the upper troposphere, so that their impacts are large in the upper layer where the atmosphere is dry. MODIS wind covers the Arctic and Antarctic regions where the atmospheric moisture is scarce especially during the winter. The fractional impact of the satellite

radiances is 65% for the moist total energy and 59% for the dry total energy. This suggests that the impact of satellite radiance observations is important especially in the forecast metric related to moisture.

c. Estimated impacts of each observation element

Figure 4 represents the AIRS satellite radiance impact estimates classified by each channel. Most of the channels have positive impact on the forecast. Some channels are estimated to have relatively large impacts and others show small impacts and even show small negative impacts for several channels. This information may help guide the better use of the satellite radiances. Figure 4 also shows the estimates using the dry total energy norm. Note that the impact estimates are substantially different from the one with moist total energy. The impacts are dependent on the selection of the error metric. Therefore, one should be careful to choose an appropriate error norm to estimate the observation impacts. Compared to the result with the moist total energy, the large peaks around channel 215 to 1627 have been reduced. This suggests that these channels are sensitive to moisture forecast.

Figure 5 shows the impact of a) RAOB and b) aircraft per observation classified by the observation level. For the radiosonde observations, observations on the lower and middle troposphere have the largest impact on the forecast. On the other hand, aircraft observations on the lower troposphere have smaller impacts compared to the radiosonde observations. Figure 6 compares the average number of the assimilated radiosonde and aircraft observations per analysis time. Horizontal distributions of the radiosonde observations are almost the same as at 600 – 800 hPa and at 125 – 250 hPa. For the aircraft observations, the distributions are completely different. Observations at 125 –

250 hPa are spread widely along the major flight tracks over data-sparse regions. However, aircraft observations in the lower troposphere are only distributed around the airports and are much denser than the radiosonde observations. This geographical distribution of the aircraft observations in the lower troposphere and near airports that often have other conventional observations seems to limit their impacts on NWP.

Observation impact estimates also provide the geographical distribution of the impact and relative importance of the observations. Figure 7 shows the average impacts of radiosonde per profile from fixed land stations in this experimental period. Overall, observations from most of the stations have positive impacts. Relatively large impacts are seen in the Tropics and also in Canada, Australia and South America.

Figure 8 shows the comparison of the radiosonde observations from two neighboring stations (Narssassuaq and Egedesminde in Greenland). Compared to the observations from Egedesminde, observations from Narssassuaq have large negative impact especially for temperature and wind observations on troposphere. Figure 8b and 8c show the statistics of observation minus the first guess of temperature and wind speed. Both statistics show the larger standard deviation for Narssassuaq. It does not automatically determine that the observations from this station have poor quality, but these observations do seem to have a detrimental impact on the short-range GFS forecast.

5. Estimation and attribution of short-range regional forecast failures

The operational NWP forecasts sometimes fail despite their relatively high average performance over the short-range forecasts. For the operational NWP centers, it is critical

to minimize the occurrence of such bad forecasts, and if possible take corrective measures. Observation impact estimates may help finding a possible cause of large short-range forecast errors in some of the cases.

In order to explore this potential use, local 24 and 30 hour forecast errors with the moist total energy norm were computed over regions of 30^o by 30^o areas covering the whole globe with 10^o increments for both latitude and longitude. For this purpose, cases of local forecast failure were identified as failures if the following conditions were satisfied: 1) The 24 hour forecast error was larger than twice its time average, and 2) The 24 hour forecast error was larger than 1.2 times of the error of 30 hour forecast from the previous analysis. Table 2 shows the list of the identified cases. If the neighboring areas on the same initial time also meet the criteria, they are considered to be the same case and only the area with the highest error times error increase is shown in the table (the number of identified areas is also shown). With these criteria, we identified 7 cases of local short-range forecast failures in this period.

Observation impacts are estimated targeting these local forecast failures. The top 1 or 2 observation types estimated to have large negative impacts are removed from the observation datasets. These “denied” observations are selected locally based on their impact distribution so that the denial does not create a large difference on other areas. Then, the analysis and the 24 hour forecast are reprocessed with the new observation sets. Table 2 also shows the denied observations and change of the 24 hour forecast error in the data denial experiment. The local forecast errors are in fact reduced in all 7 cases by the observation denial.

The left panel of figure 9 shows the 24 hour forecast error of 500 hPa geopotential height around the arctic region from the original analysis on 18 UTC February 6, 2012. There is a large forecast error associated with the trough over the Russian arctic coast. Figure 9 (middle panel) also shows the forecast change due to the removal of the MODIS polar wind observations in the data-denial experiment. The forecast error of this trough is made larger by the assimilation of the MODIS polar winds observations, validating the observation impact estimates. Since there is another local forecast failure at this analysis time and MODIS winds are estimated to have detrimental impact in both cases, suggests that MODIS wind observations on this analysis time may have had a problem. The right panel of figure 9 shows the projection of the innovation of MODIS observations to the forecast change derived from

$$-\left(\overline{\mathbf{x}}_t^f - \overline{\mathbf{x}}_t^{f-part}\right) \approx -\mathbf{M}\mathbf{K}\delta\mathbf{y}_o^{part} \approx -\mathbf{X}_t^f\left(\mathbf{H}\mathbf{X}_0^a\right)^{\mathrm{T}}\mathbf{R}^{-1}\delta\mathbf{y}_o^{part}, \tag{9}$$

where the superscript 'part' means the partial set of the observations. Equation (9) uses the same approximation used in equation (6). It is much more computationally efficient than the data denial experiment provided that one already has ensemble forecast from the EnKF analysis. The example shown in figure 9 indicates that equation (9) indeed captures quite well the actual forecast change, validating the approximation in the equations (6) and (9). Projection on the ensemble perturbations like equation (9) should be very useful especially when the size of the partial observation set is small.

6. Summary and discussion

Observation impact estimates within the GFS/EnKF have been investigated using the formulation of Kalnay et al. (2012). Assimilating all observations used in the operational

global analysis (except for TRMM/TMI precipitation retrievals), the observation impacts are estimated for each observation type. Satellite radiance observations are estimated to be most important in reducing the short-range forecast error especially for moisture. However, other observations such as aircraft observations, radiosonde, marine surface observations and scatterometer winds are also very important. The last two observation types have large impacts especially when the impacts per observation are measured.

Classified with the observation types and conditions, some examples of the advantages and disadvantages of each observing system are shown. Aircraft observations in the lower troposphere have smaller impacts per observation than the radiosondes probably because of their geographical distribution. Estimated impacts of AIRS channels show large positive impacts on the moisture and dynamical variables for many channels, and small negative impacts for a few moisture channels, possibly indicating that the radiances are not optimally assimilated. This information may guide the improvement of the use of observations in the data assimilation and possibly the design of the observation network. Continuous monitoring like Naval Research Laboratory (NRL) and National Aeronautics and Space Administration / Global Modeling and Assimilation Office (NASA/GMAO) do with the adjoint-based impact estimates may be beneficial in the operational NWP system to detect the assimilated observations with poor quality.

We developed simple criteria to detect cases of “short range regional forecast failures”, indicating that the 24 hr forecast be significantly worse than average, and worse than the 30 hour forecast started 6 hr earlier. An analysis of cases of local short-range forecast failure indicates that these observation impact estimates can be used as a tool to identify those observations that may have caused the large forecast errors. The projection

of the observational innovation on the forecast change agrees well with the corresponding data denial experiment, validating the approximation made on the formulation of the observation impact estimates. We note that identifying short-range (12 or 24 hr) forecast failures would make possible a more proactive QC approach where poor observations are withdrawn and the analysis recomputed in time to improve longer forecasts. Such early identification of flawed observations may guide studies to improve the algorithms with which they are generated.

Although the application of this method is limited to ensemble based data assimilation systems, there are many possible applications as several of the operational NWP systems are transitioning to hybrid ensemble and variational data assimilation system. One possible application is to use this method as an QC scheme as described above. Ensemble perturbations from the hybrid analysis and forecasts may also be used as inputs of the observation impact estimates. Further investigation in this promising area is warranted.

Acknowledgments.

The authors thank Daryl Kleist (NCEP/EMC) for valuable discussion and his continuous encouragement of this work, and Dr. Mitch Goldberg for his support of this research. The EnKF data assimilation system used in this study was first developed by Jeff Whitaker (NOAA/ESRL). We appreciate Ricardo Todling (NASA/GMAO) for discussions and suggestions that helped us to understand better this method. This work was partially supported by a NESDIS/JPSS JPSS Proving Ground (PG) and Risk Reduction (RR) CICS Grant.

References

Ancell, A. and Hakim, G. J. 2007. Comparing adjoint- and ensemble-sensitivity analysis with applications to observation targeting. *Mon. Wea. Rev.*, **135**, 4117-4134.

Anderson, J. L. 2001. An ensemble adjustment Kalman filter for data assimilation. *Mon. Wea. Rev.*, **129**, 2884-2903.

Bishop, C. H., Etherton, B. J. and Majumdar, S. J. 2001. Adaptive sampling with the ensemble transform Kalman filter. Part I: Theoretical aspects. *Mon. Wea. Rev.*, **129**, 420-436.

Bouttier, F. and Kelly, G. 2001. Observing-system experiments in the ECMWF 4D-Var data assimilation system. *Quart. J. Roy. Meteor. Soc.*, **127**, 1469-1488.

Cardinali, C. 2009. Monitoring the observation impact on the short-range forecast. *Quart. J. Roy. Meteor. Soc.*, **135**, 239-250.

Ehrendorfer, M., Errico, R. M. and Raeder, K. D. 1999. Singular-vector perturbation growth in a primitive equation model with moist physics. *J. Atmos. Sci.*, **56**, 1627-1648.

Gaspari, G. and Cohn, S. E. 1999. Construction of correlation functions in two and three dimensions. *Quart. J. Roy. Meteor. Soc.*, **125**, 723-757.

Hunt, B. R., Kostelich, E. J. and Szunyogh, I. 2007. Efficient Data Assimilation for Spatiotemporal Chaos: a Local Ensemble Transform Kalman Filter. *Physica D*, **230**, 112-126.

Kalnay, E., Ota, Y., Miyoshi, T. and Liu, J. 2012. A simpler formulation of forecast sensitivity to observations: application to ensemble Kalman filters. *Tellus*, **64A**, 18462, http://dx.doi.org/10.3402/tellusa.v64i0.18462.

Kunii, M., Miyoshi, T. and Kalnay, E. 2012. Estimating impact of real observations in regional numerical weather prediction using an ensemble Kalman filter. *Mon. Wea. Rev.*, **140**, 1975-1987.

Langland, R. H. and Baker, N. L. 2004. Estimation of observation impact using the NRL atmospheric variational data assimilation adjoint system. *Tellus*, **56A**, 189-201.

Li, H., Liu, J. and Kalnay, E. 2010. Correction of 'Estimating observation impact without adjoint model in an ensemble Kalman filter'. *Quart. J. Roy. Meteor. Soc.*, **136**, 1652-1654.

Liu, J. and Kalnay, E. 2008. Estimating observation impact without adjoint model in an ensemble Kalman filter. *Quart. J. Roy. Meteor. Soc.*, **134**, 1327-1335.

Majumdar, S. J., Bishop, C. H., Etherton, B. J. and Toth, Z. 2002. Adaptive sampling with the ensemble transform Kalman filter. Part II: Field program implementation. *Mon. Wea. Rev.*, **130**, 1356-1369.

Toth, Z., Szunyogh, I., Bishop, C., Majumdar, S., Morss, R., Moskaitis, J., Reynolds, D., Weinbrenner, D., Michaud, D., Surgi, N., Ralph, M., Parrish, J., Talbot, J., Pavone, J. and Lord, S. 2002. Adaptive observations at NCEP: Past, present, and future. In Proceedings of the symposium on observations, data assimilation, and probabilistic prediction, 13-17 January 2002, Orlando, Florida. American Meteorological Society, Boston, USA.

Whitaker, J. S. and Hamill, T. M. 2002. Ensemble data assimilation without perturbed observations. *Mon. Wea. Rev.*, **130**, 1913-1924.

Whitaker, J. S., Hamill, T. M., Wei, X., Song, Y. and Toth, Z. 2008. Ensemble data assimilation with the NCEP global forecast system. *Mon. Wea. Rev.*, **136**, 463-482.

Zapotocny, T. H., Jung, J. A., Marshall, J. F. L. and Treadon, R. E. 2007. A two-season impact study of satellite and in situ data in the NCEP Global Data Assimilation System. *Wea. Forecasting*, **22**, 887-909.

Zapotocny, T. H., Jung, J. A., Marshall, J. F. L. and Treadon, R. E. 2008. A two-season impact study of four satellite data types and rawinsonde data in the NCEP Global Data Assimilation System. *Wea. Forecasting*, **23**, 80-100.

Zhu, Y. and Gelaro, R. 2008. Observation sensitivity calculations using the adjoint of the Gridpoint Statistical Interpolation (GSI) analysis system. *Mon. Wea. Rev.*, **136**, 335-351.

List of Figures

FIG. 6. Average number of assimilated radiosonde observations a) from 250 to 125 hPa, b) from 800 to 600 hPa and aircraft observations c) from 250 to 125 hPa and d) from 800 to 600 hPa in each 5^{o} by 5^{o} area on 1 analysis.

FIG. 7. Average impact (moist total energy, J kg^{-1}) of 1 radiosonde profile from the fixed land stations. Only the stations that have more than 20 profiles in the period are shown. Numbers 4220 (Egedesminde) and 4270 (Narssassuaq) indicate the location of the stations shown in Fig. 8 and 9.

FIG. 8. Comparison of the radiosonde observations from Narssassuaq (red line, 4270) and Egedesminde (blue line, 4220) showing a) average impacts (J kg^{-1}) of each observation element (solid: temperature, dashed: winds, dotted: humidity) on each pressure level by 1 profile and observation departure statistics (dashed: bias, solid: standard deviation) of b) temperature (K) and c) wind speed (m s^{-1}).

FIG. 9. 24 hour forecast error of 500 hPa geopotential height (unit: m, 18 UTC February 6, 2012 initial) from original analysis (left) and forecast change due to the removal of the observations (MODIS polar wind in 60N~90N, 30E~90E) in the data denial experiment (middle: actual change and right: projection on the ensemble perturbations). Black contours show the analysis. Magenta cones show the target area of the observation impact estimate.

TABLE 1. Observation types assimilated in the experiment. The third column shows the average number of observations assimilated on 1 analysis (in thousands). u, v, T, q and Ps represents u and v wind components, temperature, specific humidity and surface pressure, respectively.

Type of data	Description	Number (thousands)
Aircraft	u, v, and T observations from the aircrafts	173
Radiosonde	Radiosonde observations (u, v, T, q and Ps)	55
Satellite_Wind	Atmospheric Motion Vectors (u and v) from geostationary satellites	96
GPSRO	GPS radio occultation	95
Land-Surface	Ps observations from land surface stations	54
Marine-Surface	Surface u, v, T, q and Ps observations from the buoys and ships	23
MODIS_Wind	Atmospheric Motion Vectors (u and v) from MODIS	36
ASCAT_Wind	u and v observations from ASCAT scatterometer over ocean	17
PIBAL	u and v observations from pilot balloons	1.9
NEXRAD_Wind	u and v observations from the NEXRAD (radar)	14
Profiler_Wind	u and v observations from the wind profilers	12
Dropsonde	Flight-level reconnaissance and dropsonde (u, v, T and q)	0.2
WINDSAT_Wind	u and v observations from ASCAT scatterometer over ocean (super observation)	0.8
TCVital	Pseudo surface pressure observations at tropical cyclone storm center	0.0006
Ozone	Ozone retrievals from satellite radiances	14
AMSUA	Satellite microwave sounder radiances (from 5 satellites)	586
IASI	Satellite infrared hyper spectral sounder radiances	1143
Aqua_AIRS	Satellite infrared hyper spectral sounder radiances	630
ATMS	Satellite microwave sounder radiances (from Suomi-NPP)	150
HIRS	Satellite infrared radiances (from 2 satellites)	119
MHS	Satellite microwave sounder radiances (from 3 satellites)	67
GOES	GOES infrared sounder radiances (GOES13 and 15)	40
SEVIRI	SEVIRI clear sky radiances	6.1

TABLE 2. List of local 24 hour forecast failure cases (initial time from 00 UTC January 8, 2012 to 18 UTC February 7, 2012). Third, fourth and fifth columns show the forecast error size normalized with the time averaged error, the rate of the error size compared with the error of 30 hour forecast from the previous analysis, and the number of areas that meet the criteria. Sixth column shows the denied observation based on the observation impact estimates and seventh column shows the change of the 24 hour local forecast error for observation denial experiment. The case shown in bold font is an example shown in Fig. 8 and 9.

Initial	Area	Size	Rate	N	Denied observation	Change
12 UTC JAN 10	90S~60S 100E~130E	2.04	1.20	1	GPSRO (80S~60S, 90E~120E) ASCAT (60S~50S, 100E~120E)	-6.6%
06 UTC JAN 12	50N~80N 150E ~ 180	2.18	1.40	1	AMSUA (ch4: 45N~75N, 160E~170W, ch5:40N~55N, 155E~180, NOAA15 ch6: 50N~75N, 140E~170W, ch7: 70N~80N, 130E~170E)	-11.4%
00 UTC JAN 16	30N~60N 30W~0	2.13	1.31	2	Radiosonde wind (Valentia, Ireland), ASCAT (40N~47N, 20W~10W, 50N~55N, 35W~30W)	-1.0%
12 UTC JAN 22	90S~60S 130E~160E	2.34	1.22	2	AMSUA (ch5: 65S~50S, 90E~110E, 60S~50S, 120E~127E, ch6: 60S~45S, 110E~125E)	-2.2%
06 UTC FEB 2	50N~80N 150W~120W	3.10	1.32	4	IASI (35N~45N, 155W~150W) NEXRAD (55N~60N, 160W~135W)	-5.5%
18 UTC FEB 6	**60N~90N 50E~80E**	**2.06**	**1.71**	**2**	**MODIS_Wind (60N~90N, 30E~90E)**	**-39.0%**
18 UTC FEB 6	90S~60S 20W~10E	3.56	1.22	1	MODIS_Wind (80S~50S, 30W~0)	-22.5%

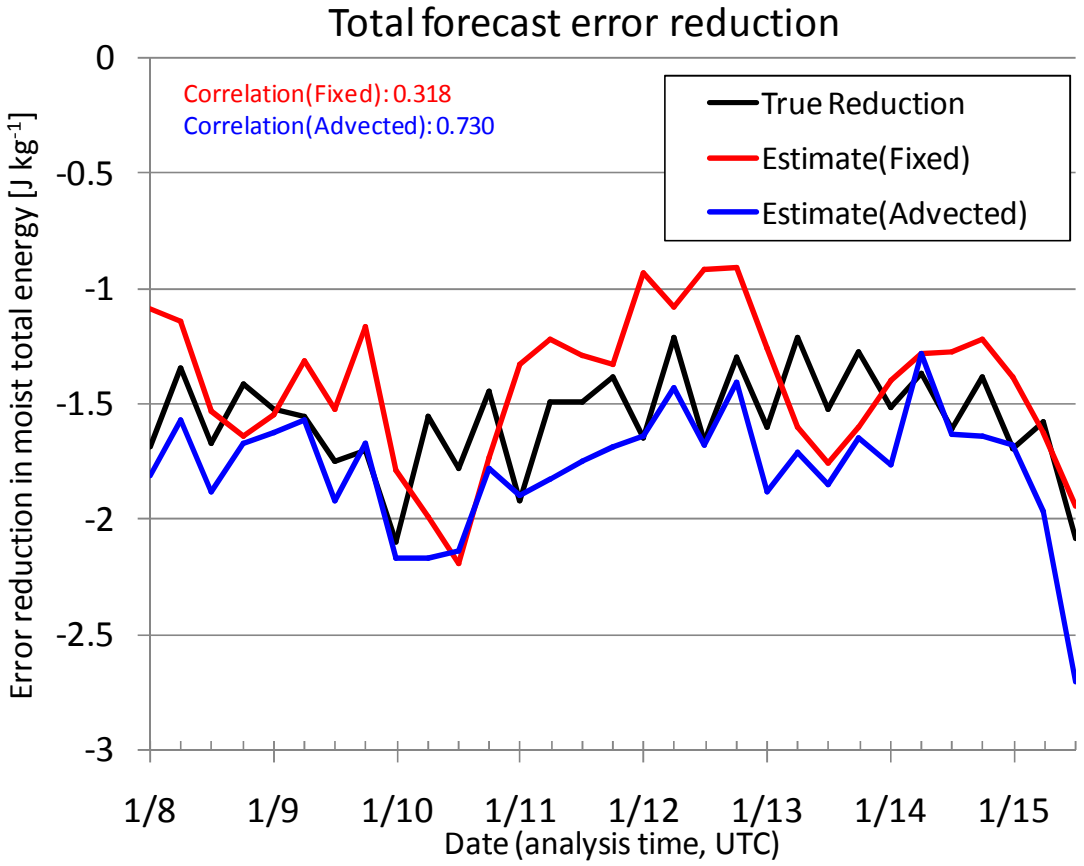

FIG. 1. Time series of the total forecast error reduction of each estimate (unit: J kg^{-1}). Black, red, and blue lines show the actual forecast error reduction verified against the own analysis, estimated error reduction from the EnKF-based method with fixed localization (Fixed), and with moving localization (Advected). Numbers on upper left corner show the correlation of each estimate to the actual forecast error reduction.

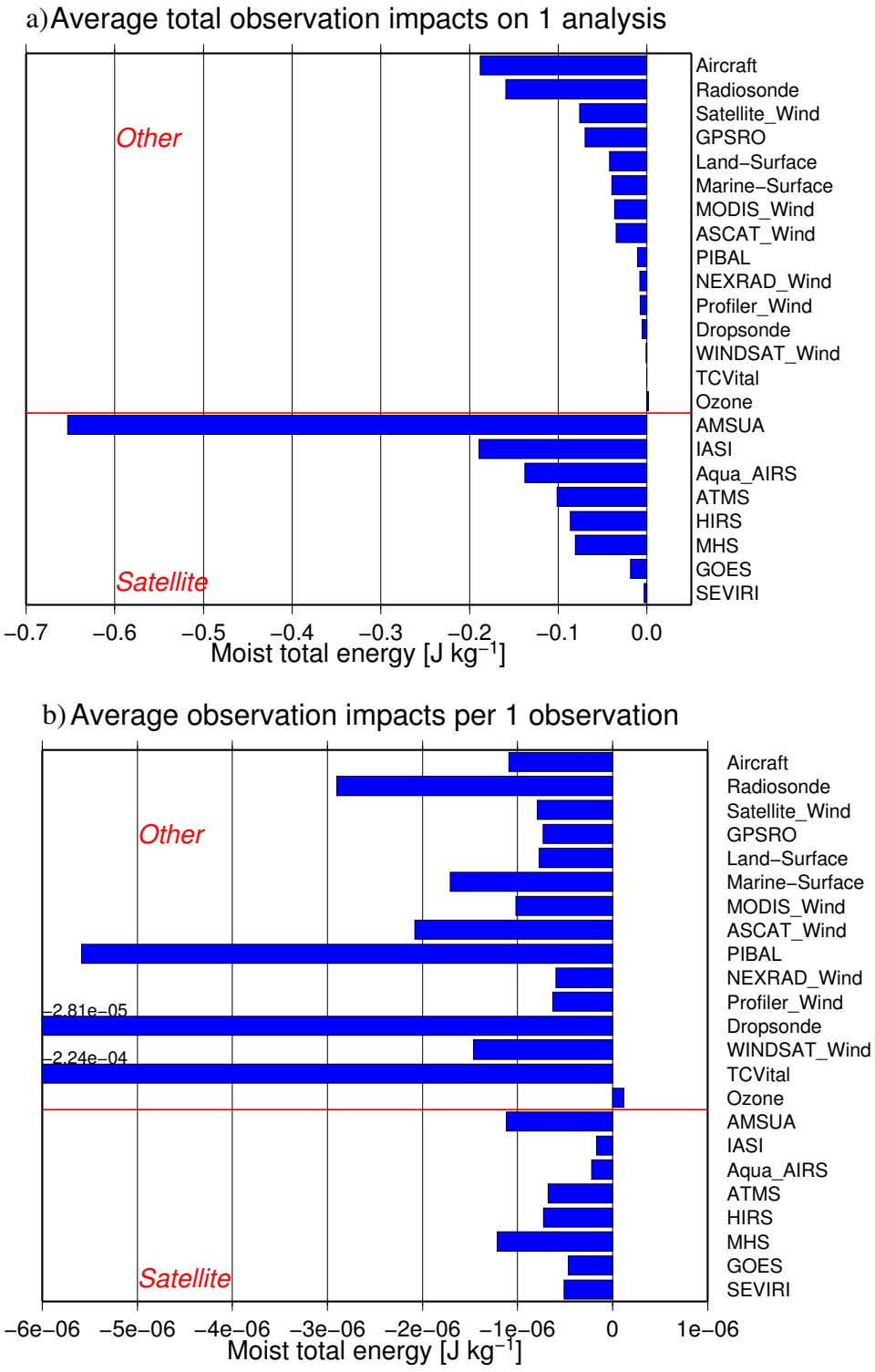

FIG. 2. Estimated average 24 hour forecast error reduction contributed from each observation types (moist total energy, J kg^{-1}). a) represents the total error reduction and b) represents error reduction per 1 observation.

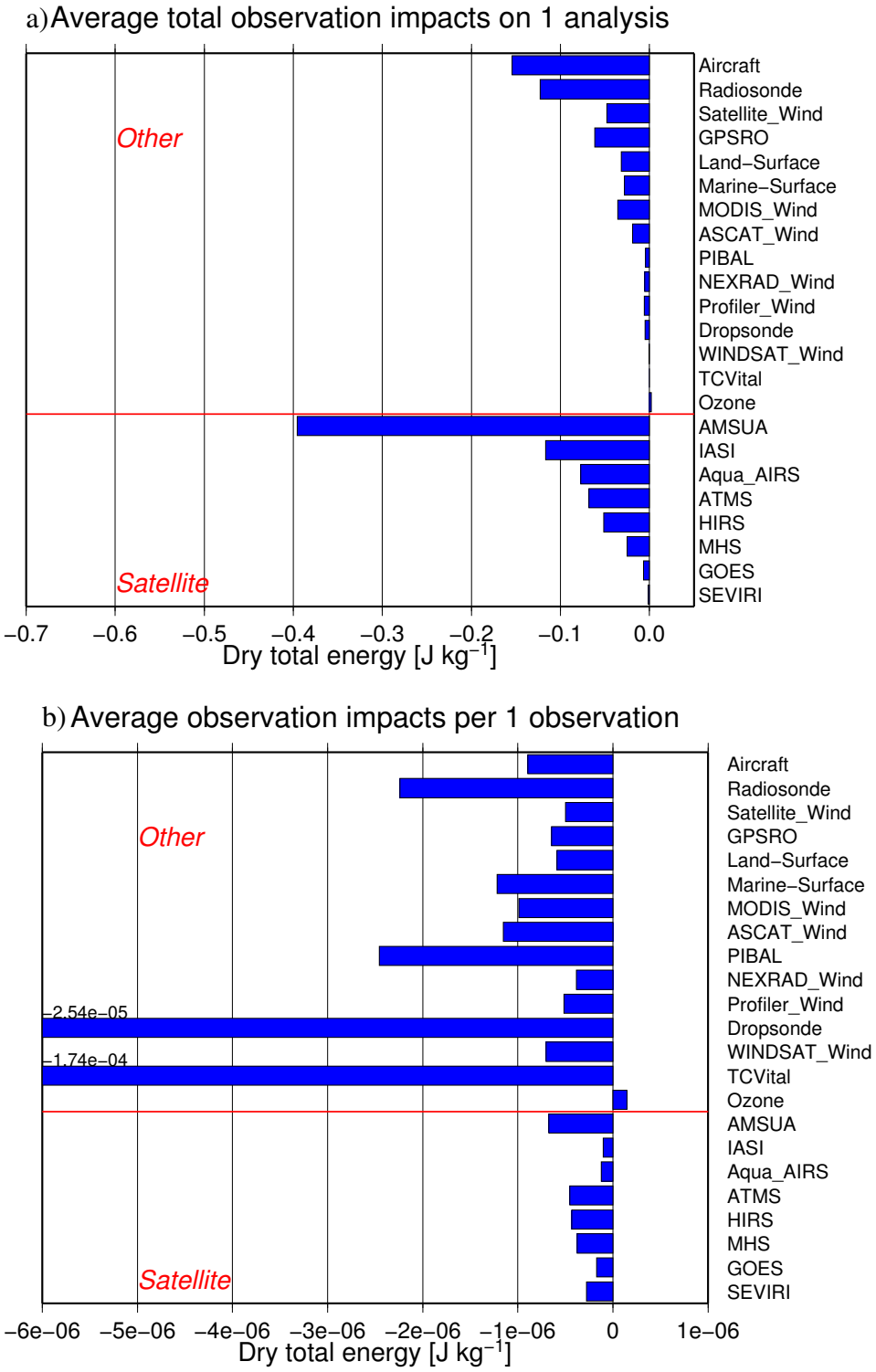

FIG. 3. Same as Fig. 2 but with the dry total energy norm (J kg^{-1}).

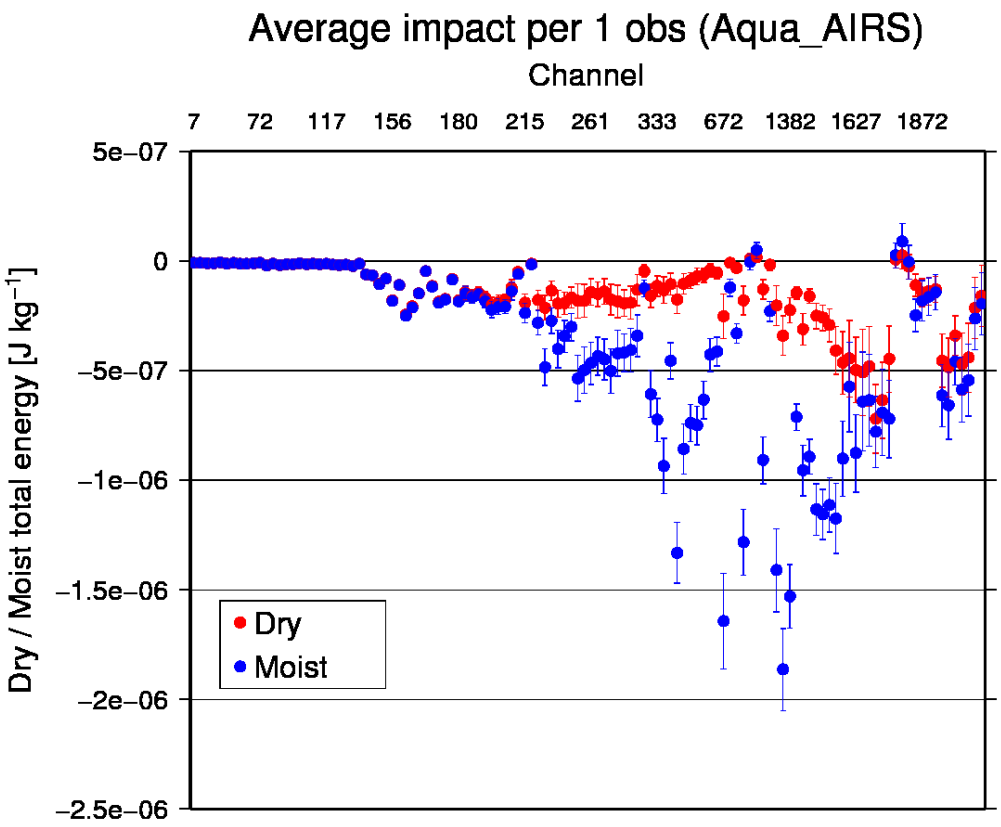

FIG. 4. Estimated AIRS satellite radiance observation impacts classified by each channels with the dry total energy (red, J kg^{-1}), and the moist total energy (blue, J kg^{-1}). Estimated forecast error reduction by 1 observation is shown. Vertical bars represent the 95 % confidence interval of the average values.

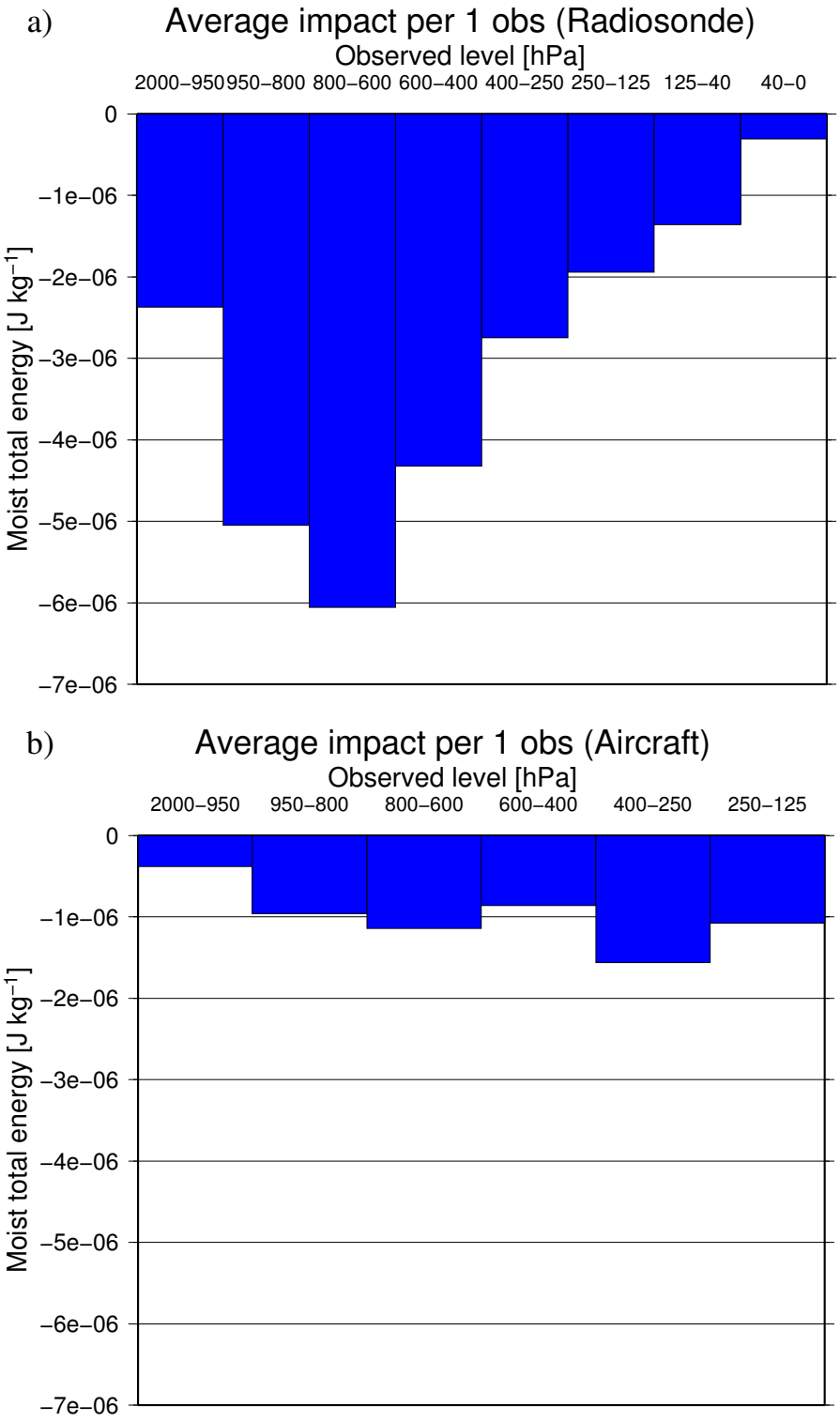

FIG. 5. Estimated average observation impacts of a) radiosonde and b) aircraft classified by observed level (moist total energy, J kg^{-1}). Estimated forecast error reduction by 1 observation is shown.

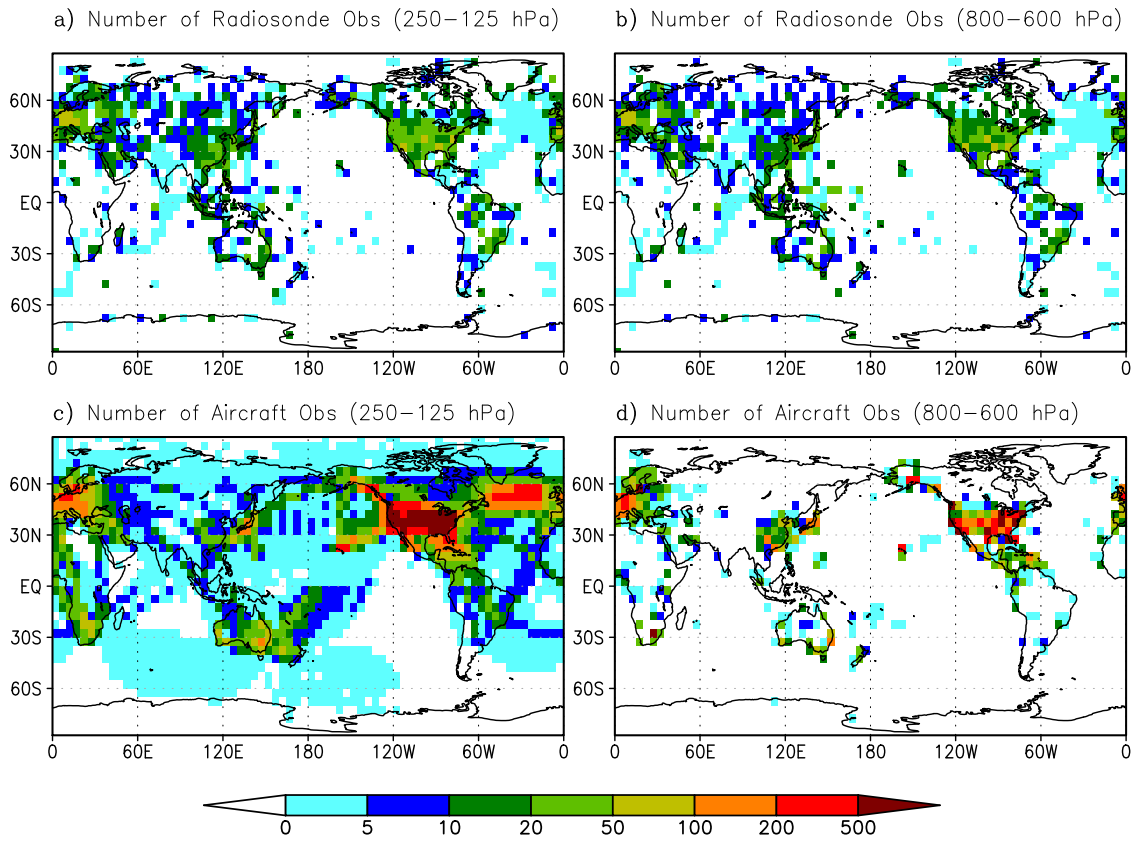

FIG. 6. Average number of assimilated radiosonde observations a) from 250 to 125 hPa, b) from 800 to 600 hPa and aircraft observations c) from 250 to 125 hPa and d) from 800 to 600 hPa in each 5^{o} by 5^{o} area on 1 analysis.

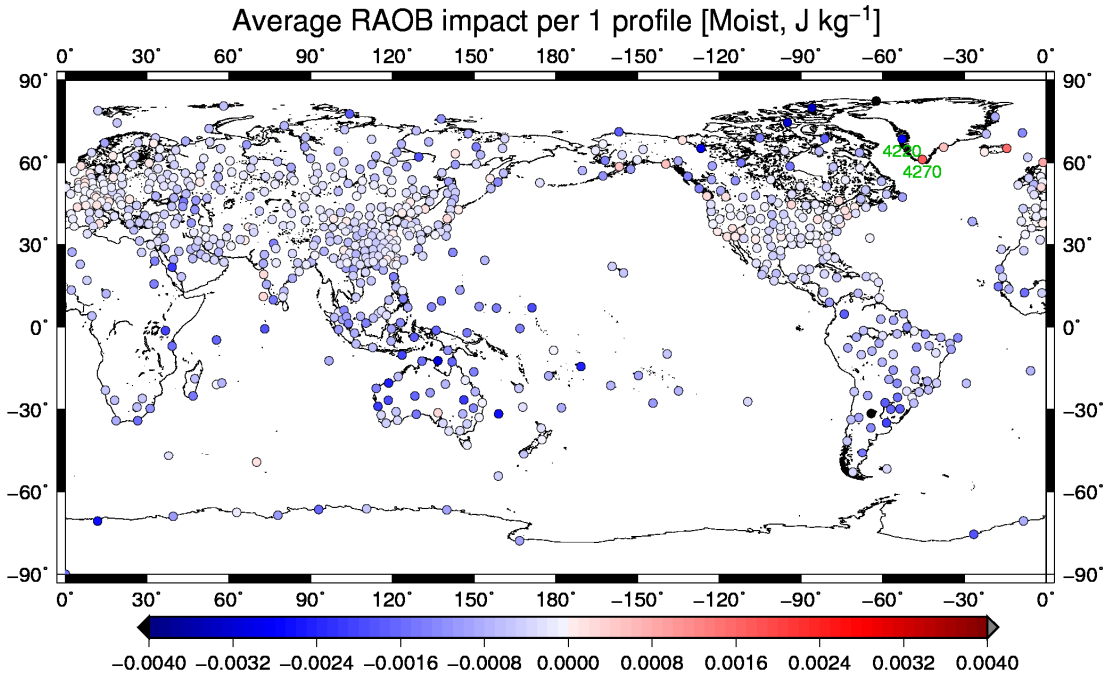

FIG. 7. Average impact (moist total energy, J kg^{-1}) of 1 radiosonde profile from the fixed land stations. Only the stations that have more than 20 profiles in the period are shown. Numbers 4220 (Egedesminde) and 4270 (Narssassuaq) indicate the location of the stations shown in Fig. 8 and 9.

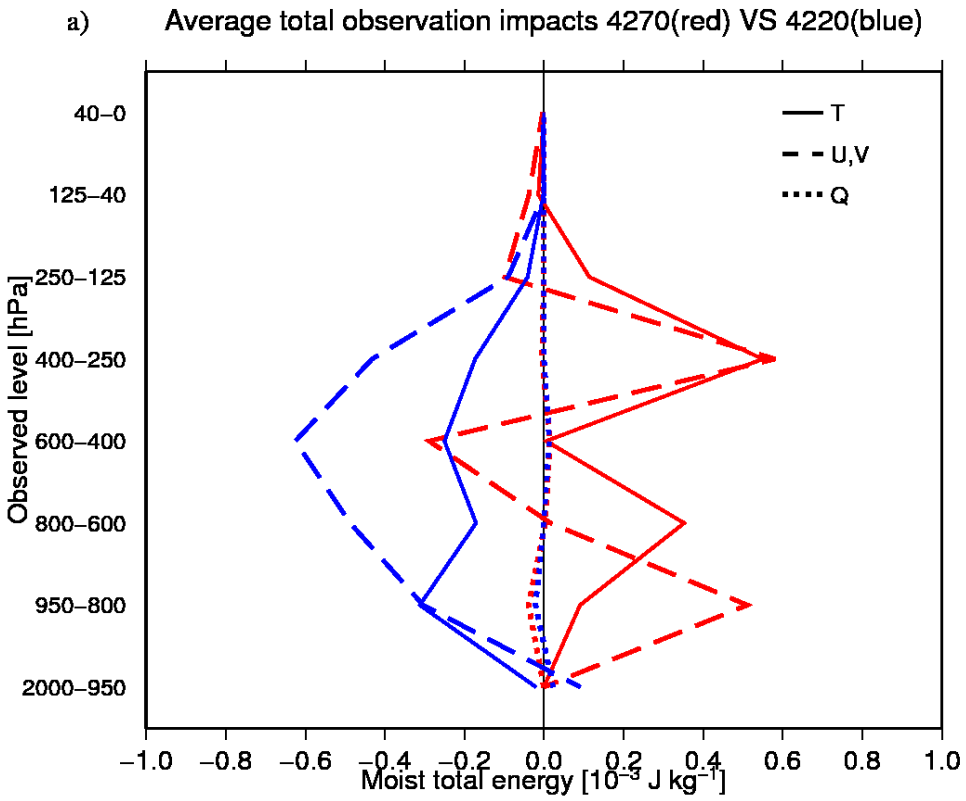
a)
Average total observation impacts 4270(red) VS 4220(blue)
T
U,V
Q
Observed level [hPa]
40–0
125–40
250–125
400–250
600–400
800–600
950–800
2000–950
–1.0 –0.8 –0.6 –0.4 –0.2 0.0 0.2 0.4 0.6 0.8 1.0
Moist total energy [10–3 J kg–1]

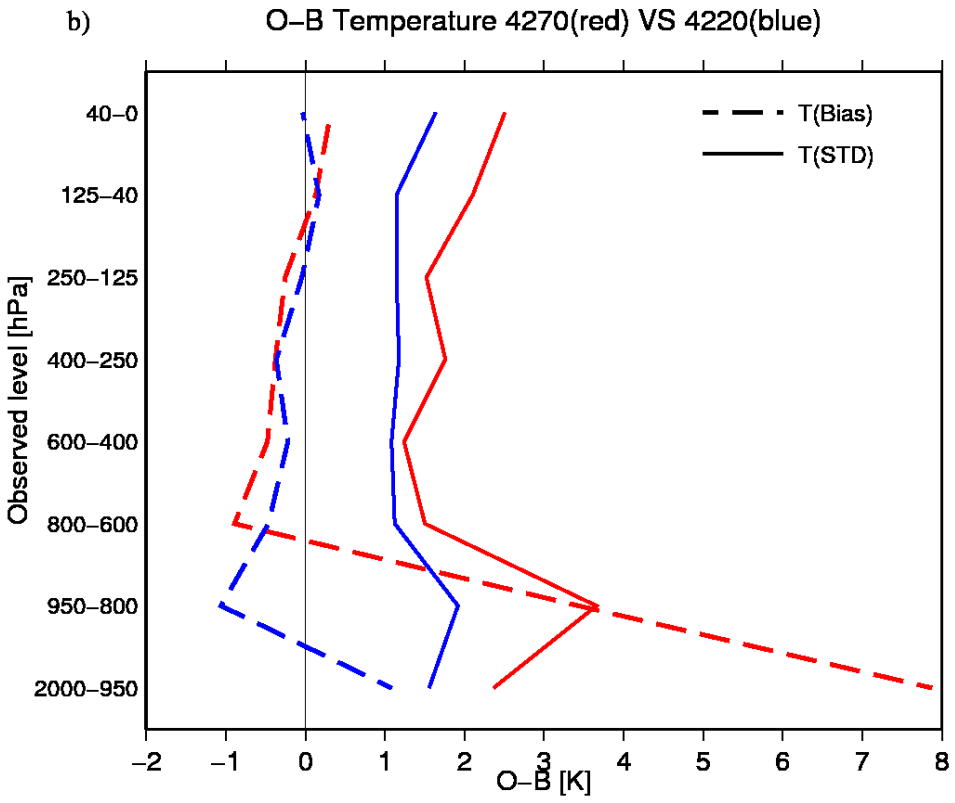
b)
O–B Temperature 4270(red) VS 4220(blue)
T(Bias)
T(STD)
Observed level [hPa]
40–0
125–40
250–125
400–250
600–400
800–600
950–800
2000–950
–2 –1 0 1 2 3 4 5 6 7 8
O–B [K]

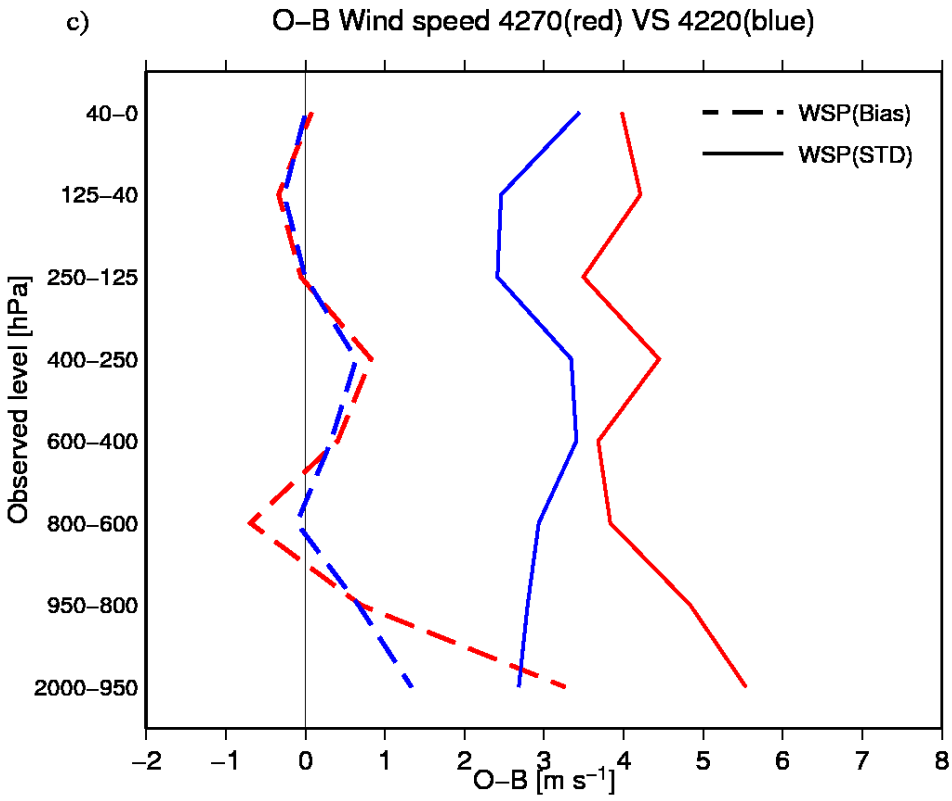

FIG. 8. Comparison of the radiosonde observations from Narssassuaq (red line, 4270) and Egedesminde (blue line, 4220) showing a) average impacts (J kg^{-1}) of each observation element (solid: temperature, dashed: winds, dotted: humidity) on each pressure level by 1 profile and observation departure statistics (dashed: bias, solid: standard deviation) of b) temperature (K) and c) wind speed (m s^{-1}).

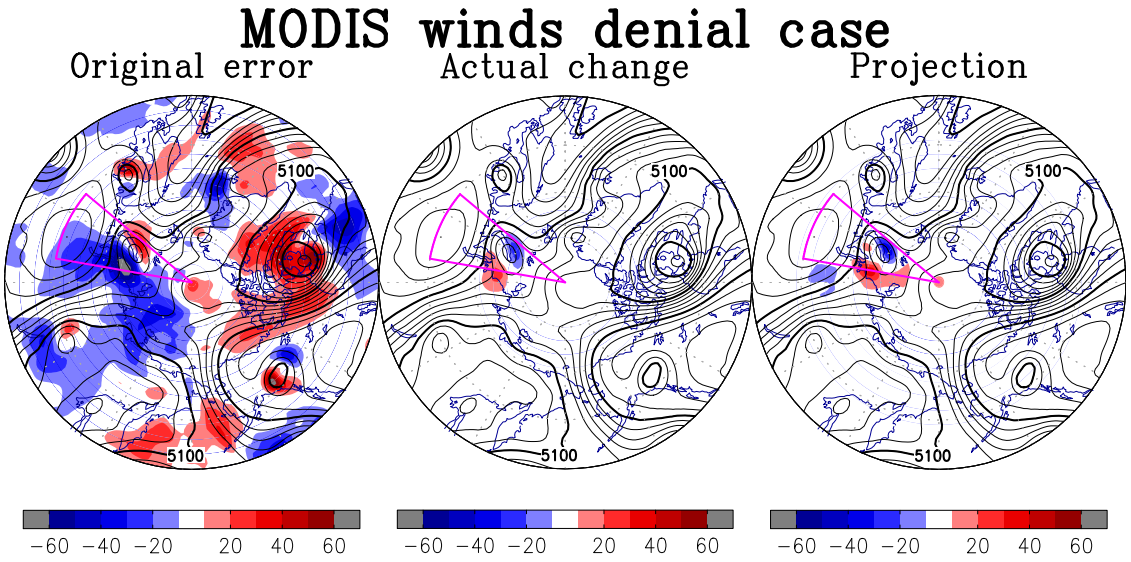

FIG. 9. 24 hour forecast error of 500 hPa geopotential height (unit: m, 18 UTC February 6, 2012 initial) from original analysis (left) and forecast change due to the removal of the observations (MODIS polar wind in 60N~90N, 30E~90E) in the data denial experiment (middle: actual change and right: projection on the ensemble perturbations). Black contours show the analysis. Magenta cones show the target area of the observation impact estimate.